Multiple-stepped Zeeman field offset method applied in acquiring enhanced resolution spin-echo electron paramagnetic resonance images

Payam Seifi, Boris Epel, Colin Mailer, and Howard J. Halpern[a)]
Department of Radiation and Cellular Oncology, Center for EPR Imaging In Vivo Physiology, University of Chicago, Chicago, Illinois 60637

(Received 14 April 2010; revised 4 June 2010; accepted for publication 8 July 2010; published 28 September 2010)

Purpose: Electron paramagnetic resonance (EPR) imaging techniques provide quantitative *in vivo* oxygen distribution images. Time-domain techniques including electron spin echo (ESE) imaging have been under study in recent years for their robustness and promising new features. One of the limitations of ESE imaging addressed here is the finite acquisition frequency bandwidth, which imposes limits on applied magnetic field gradients and the resulting image spatial resolution. In order to improve the image spatial resolution, we have extended the effective frequency bandwidth of the imaging system by acquiring projections at multiple Zeeman magnetic field offsets and combining them to restore complete projections obtained with more uniform frequency response, resulting in higher quality images.

Methods: In multiple-stepped magnetic field or multi-B scheme, every projection of the three dimensional object is acquired at different main or Zeeman magnetic field (B) offset values. The data from field offset steps are combined, normalizing to the imaging system frequency acquisition window function, a sensitivity profile, to restore the complete projection. A multipurpose pulse EPR imager and phantoms containing the same type of spin probe (OX063H) used in routine animal imaging were also used in this study.

Results: Using the multi-B method, we were able to acquire images of our phantoms with enhanced spatial resolution compared to the conventional ESE approach. Compared to standard single-B ESE images, the T_2 resolutions of multi-B images were superior using a high spatial-resolution regime. Image artifacts present in high-gradient single-B ESE images are also substantially reduced using in the multi-B scheme.

Conclusions: The multi-B method is less susceptible to instrumental limitations for larger gradient fields and acquiring images with higher spatial resolution better overall quality, without the need to alter the existing pulse ESE image acquisition hardware. [DOI: 10.1118/1.3475936]

Key words: electron paramagnetic resonance imaging, electron spin echo, multi-B method, frequency bandwidth, spatial resolution

I. INTRODUCTION

In the past few decades *in vivo* electron paramagnetic resonance (EPR) imaging has shown to be capable of providing valuable information regarding the three dimensional oxygen distributions in tumor and normal tissue in small animals.[1–8] Knowledge of oxygen partial pressure or pO_2 is of great radiobiological interest and can have great impact in radiation therapy planning in solid tumor cancer treatment.[9] EPR imaging provides a means to measure pO_2 rapidly and minimally invasively, by directly injecting spin probe in the bloodstream and gathering information about local oxygen tension based on changes detected in the electron spin spectrum at every location in the tissue.

Traditionally the continuous wave (cw) methods have been studied more extensively, both due to low radiofrequency (rf) power requirements and the wide range of radicals that can be imaged. One of the drawbacks of the conventional cw EPR imaging is the acquisition speed, which is constrained by the need to sweep the magnetic field.[4,6] The problem has been addressed by using rotating magnetic field gradients[10–12] and developing rapid-scan EPR techniques.[13–15] On the other hand, pulse EPR techniques, such as those using projection reconstruction from free induction decay or echo detected signals, or k-space sampling in the case of single-point imaging (SPI) are proving to be efficient in obtaining fast images.[16,17] In time-domain EPR imaging, there is usually no need to sweep the main magnetic field, and ideally all spectral frequency components are present in the acquired time-domain trace. Moreover, in projection based techniques such as electron spin echo, only the direction and not the magnitudes of magnetic field gradients need to change to acquire spatial information,[5,18] which makes them even more suitable for fast image acquisition compared to SPI imaging where full three dimensional sampling of the frequency space with gradients is required. An additional advantage for electron spin echo (ESE) imaging is direct T_2 sensitivity. The work presented here focuses on ESE imaging (Fig. 1).

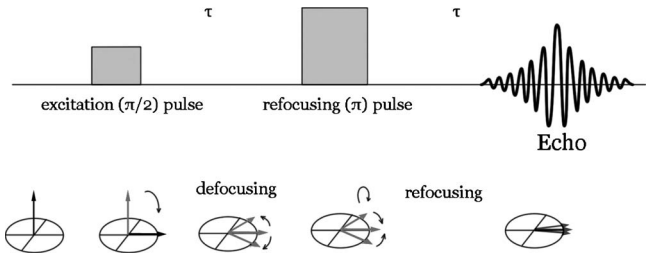

FIG. 1. ESE is done using one excitation (90° or $\pi/2$) and one refocusing (180° or π) pulse.

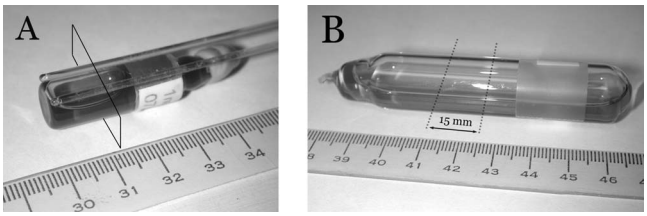

FIG. 2. Imaging phantoms. (a) The 1 mM OX063 bottle phantom with two capillary tubes. The plane shows the cross section of the phantom that will be shown in Figs. 3 and 4. (b) The tube phantom containing 200 μM concentration of Finland trityl used for 1D experiments. The dotted lines represent the section inside the resonator.

A major source of spatial blurring of EPR images is spectral linewidth of the electron spin species resulting mostly from the hyperfine interactions. The ESE image spatial resolution is constrained by the strength of magnetic field gradients that can be applied. Larger applied gradients decrease the effect of hyperfine induced blurring by proportionally stretching projections in the frequency space without affecting hyperfine splittings, therefore fractionally sharpening projections and the image. On the other hand, applying large gradients can result both in signal to noise ratio (SNR) reduction and data truncation if the frequency span of the object becomes larger than the imaging system frequency bandwidth. The imager bandwidth is mostly determined by the resonator quality factor, applied pulse shape, and bandwidth of individual components of the detection system. To avoid such truncation effects, the gradient magnitude and object size should be carefully matched to the imager bandwidth. For instance, in order to image a 2 cm size object with 10 MHz frequency bandwidth limit, the magnitude of the gradient that can be applied with no severe data truncation is of order of 10 MHz/(0.02 m$\times$28 MHz/mT) or 20 mT/m, where 28 MHz/mT is γ or gyromagnetic ratio of the free electron. For a spin probe with a 15 μT line width, this means that the lower bound for the image spatial resolution is about 0.75 mm.

A robust *in vivo* ESE imaging system currently used in our laboratory for small animal imaging was described recently.[19] Here we will show how the same imaging system can be used to acquire images with enhanced spatial and T_2 resolution, using the proposed multiple-stepped magnetic field or simply the multi-B ESE technique. Since unpaired electron spins resonate with frequencies proportional to the local magnetic field, a shift in the main field becomes equivalent to shifting the object function in the frequency space. This is the main idea behind multi-B ESE, which makes it possible to cover the frequencies present in the acquired signal from a spin system at the presence of magnetic field gradients. Therefore, the multi-B technique allows extension of the effective frequency bandwidth of the imaging system. One application for large bandwidth is high-resolution imaging, which is of interest in the study of fine-scale oxygenation patterns in tumor as well as normal tissue.

II. METHODS AND MATERIALS

II.A. Phantoms

For three-dimensional (3D) ESE imaging experiments, a partially filled sealed glass bottle with 45 mm length and 9.5 mm inner diameter containing 2 ml of deoxygenated 1 mM concentration of OX063 trityl spin probe (methyl-tris [8-carboxy-2,2,6,6-tetrakis[2-hydroxyethyl]benzo [1,2-d:4,5-d′]bis [1,3]dithiol-4-yl]-trisodium salt, GE Healthcare)[20,21] was used for our imaging experiments. Two smaller tubes made from capillary tubes with inner diameter of 1.1 mm were also placed close to the phantom bottle, in order to better illustrate the image sharpness or resolution [Fig. 2(a)]. For the one-dimensional (1D) experiment we decided to use a phantom which is uniform along the long axis of the resonator. A partially filled sealed glass tube containing deoxygenated Finland trityl spin probe (methyl-tris [8-carboxy-2,2,6,6-tetrakis[perdeuteromethyll]benzo [1,2-d:4,5-d′]bis [1,3]dithiol-4-yl]-trisodium salt, GE Healthcare)[20,21] was used. The concentration of the spin probe was 200 μM and the tube had 15 mm inner diameter, shown in Fig. 2(b). Care was taken to install the phantom fully horizontally inside the resonator in order to get a uniform spin density profile along the long axis of the resonator, for the purpose of noise profile measurements as explained later.

II.B. Pulse EPR imager

Our pulse EPR imaging system is fully described previously[19] therefore only the aspects most relevant to experiments done in this paper are described: A multipurpose pulse imager operating at 250 MHz central frequency was used for the experiment, capable of applying rf pulse peak power of up to 1 KW. The resonator used for imaging was made from acrylonitrile butadiene styrene (ABS) plastic with $\sim$40 μm-thick 3M conductive copper band taped to the surface. This was a capacitatively coupled one loop-one gap resonator of 19 mm in diameter and 15 mm in length where the resonator loop is also the sample holder. The quality factor (Q) for the empty resonator is normally about 250, suitable for cw imaging applications. Q was reduced from original value to 13.5 by installing a 750 Ω shunt resistor

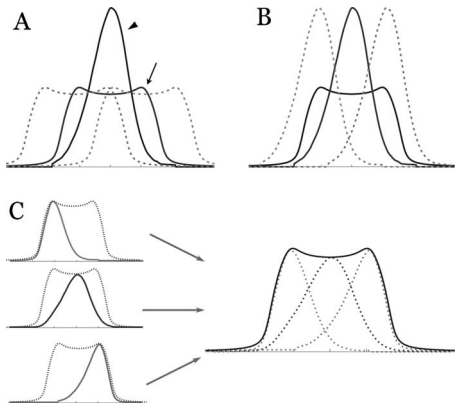

FIG. 3. The multiple-B scheme. (a) The imager acquisition window function (black arrowhead) and object function (arrow) are shown in the frequency domain. Shifted object functions due to shift in magnetic field are represented as dashed lines. (b) Equivalent representation where imager profile is shifted in opposite direction, allowing complete coverage of the object function. (c) Subprojections from each field step are combined to recover the original projection.

across the capacitative gap. This resulted in a resonator frequency bandwidth of (250 MHz/13.5) or 18 MHz at full width half maximum (FWHM) value.

II.C. Image acquisition

In all experiments electron spin echo excitation $(\pi/2)$ and refocusing (π) pulses were both 35 ns in length with a switchable power attenuator to produce a $\pi/2$ pulse with 1/4 the power of the π pulse.[22] This is an improvement compared to our earlier setup where the refocusing pulse had the same power as the excitation pulse, yet was twice longer in duration. This reduction in pulse length helps better matching the quality factor of the resonator to the pulse bandwidth, increasing the system bandwidth. The FWHM frequency bandwidth obtained for the imager using two 35 ns long pulses was ~10 MHz.

Pulse rf peak power of 200 W (for the π pulse) or 53 dBm was used in all measurements. For every gradient direction in the 3D spatial direction, time-domain data were acquired using $(\pi/2)_i-\tau-(\pi)_j-\tau$ pulse sequence, where the indices i and j refer to the phases of each pulse. Cyclically ordered phase sequence (CYCLOPS) with 16 phase cycles was used in order to reduce image artifacts.

In the previously published ESE imaging technique, the main (Zeeman) magnetic field is fixed and only gradients are changing.[19] In the proposed multi-B scheme, for every gradient projection time-domain data are acquired at multiple values of the main magnetic field offset. The general scheme is shown in Fig. 3 which illustrates that acquisition at different magnetic field offsets is equivalent to extending the frequency bandwidth of the imaging system. A complete projection is recovered by joining together subprojections acquired from each Zeeman field offset. For both conventional ESE (single-B) and multi-B schemes echo signal averaging is used to improve the SNR. In the multi-B scheme the same number of echo averages per projection are equally distributed among all subprojections. When comparing corresponding single- and multi-B images, the total number of echoes averaged per complete projection is the same.

Some of the relevant acquisition parameters for the single- and multi-B imaging protocols are given in Table I. The angular sampling numbers refers to the number of samples taken in polar and azimuthal directions (N_{Az} and N_{Polar}) of the spherical coordinates. Projection angles were sampled with equal solid angle coverage, which reduces the number of required samples by a factor of approximately 2/3 from what would be obtained using equal linear azimuthal and polar angle sampling.[23] The total number of projections is also given in Table I.

For each protocol, gradient magnitudes ranging from 10 to 30 mT/m are applied. For multi-B scheme, the field offset step size and the number of steps (N_B) are chosen in accordance with the strength of the gradient. At 10 mT/m, only three field offsets covering from −50 to +50 μT were used since the 10 MHz bandwidth is large enough to span the data; whereas for 30 mT/m imaging the field offset coverage was from −200 to 200 μT in five field steps.

Baseline signal was acquired by shifting the main field by 1.5 mT off resonance. The baseline was subtracted from on-resonance data. Due to the dynamic nature of the baseline spurious signal, baseline acquisition every four complete projections turned out to be a good trade-off point between the image quality and acquisition time overhead for both schemes.[19]

Latencies were introduced to allow for the magnetic field and/or gradients settling between projections and baseline. These include 15 ms for gradient switching, 150 ms for

TABLE I. The ESE EPRI protocol acquisition and reconstruction parameters. For each imaging protocol images with four different gradients are acquired: 15, 20, 25, and 30 mT/m.

Protocol	Angular Sampling (equal solid angle)	Acquisition time	Number of field steps (N_B), coverage	Reconstruction matrix size
ESE-SB I	16×16, 164 total	8.0 min	1 step No field offset	64×64×64×5
ESE-SB II	32×32, 654 total	31.8 min	1 step No field offset	128×128×128×5
ESE-MB I	16×16, 164 total	7.4 min	5 steps, −0.2, −0.1, 0, 0.1, 0.2 mT offsets	64×64×64×5
ESE-MB II	32×32, 654 total	29.6 min	5 steps, −0.2, −0.1, 0, 0.1, 0.2 mT offsets	128×128×128×5

switching to off-resonance field, and 250 ms for switching from off to on resonance. For multi-B images, 100 ms delay time was used for switching from one field step to the next one. Gradient coils are smaller in size and number of turns, therefore have shorter settling times. In order to reduce the time delay contribution to acquisition overhead in the multi-B method, subprojections from sequential projections and same step-B were acquired before switching to the next field step. Furthermore, off-resonance baseline projections were treated as single subprojections in the multi-B method, therefore resulting in slightly faster acquisition for multi-B images.

For the purpose of T_2 determination, time-domain data were acquired at 5 different echo times (τ), logarithmically spaced between 0.63 and 2.4 μs. The resulting five images, one from each τ, are used in determine T_2 for each image voxel, as discussed later. In order to obtain uncertainty in our T_2 resolution estimate, all experiments were performed three times.

II.D. Converting time-domain data to spatial projections

Every time-domain echo trace is composed of 1000 time points acquired from the two quadrature detection channels, i.e., real and imaginary with temporal sampling rate of 4 ns per point.

For the single-B data, first the echo position is determined by finding the maximum signal position from two channels. The phase of the signal is determined from the signal phase at the echo time, and corrected subsequently. The data acquired prior to the echo time are discarded. The last 250 points in the data are averages and subtracted from the rest of the signal, to correct for any existing dc current offsets in the data.

The echo data are then Fourier transformed to obtain frequency encoded spatial projections. Before applying the fast Fourier transform (FFT), the following processing steps are taken.

Due to the finite bandwidth of the imager, the converted data in the frequency domain are distorted by sensitivity variations as a function of frequency from the ideal projections, even at high SNR. These distortions, due to the system frequency response profile, are referred to as the acquisition window function (AWF). The acquisition window function is normally measured before or after any imaging session. The AWF is measured by stepping the magnetic field and measuring the signal amplitude at a given time. The AWF correction is derived from the AWF amplitude by inverting and regularizing to a maximum correction factor at positive and negative frequencies. This is done to avoid amplifying noise at peripheral frequencies. The frequency domain data are converted to spatial coordinates by dividing by the gradient magnitude and the electron gyromagnetic ratio. Spatial projections are passed to the image reconstruction algorithm.

For multi-B images, for each complete projection time-domain datum is assembled by combining corresponding subprojections, where subprojections are echo profiles obtained at a particular field offset and converted to the frequency domain. The echo time and the correct phase are determined based on the signal maximum position, similar to the single-B processing. Phase correction, dc baseline removal, and FFT steps are also carried out similar to single-B processing. The frequency domain data are shifted according to the field offset for each subprojection. Combining subprojection data is done by applying weighted sum of data at each overlapping frequency bin, according to the following formula:

$$S(f) = \sum_{i=1}^{N_B} \alpha_i(f), S_i(f). \tag{1}$$

Here S_i is the signal from subprojection i after Fourier transforming to the frequency domain f and α_i are the weight functions for subprojection i, as defined below, and N_B indicates the total number of subprojections for each complete projection. We used the following formula to calculate the weight function:

$$\alpha_i(f) = \frac{\mathrm{AWF}(f + \delta f_i)}{\Sigma_{j=1}^{N_B} \mathrm{AWF}^2(f + \delta f_j)}, \tag{2}$$

where δf_i indicates the frequency shift of the ith subprojection. The method is based on the sum-of-squares (SoS) approach used to optimizes the SNR in each frequency bin when the system noise is fully stochastic and uniform.[24] While the system noise is neither fully stochastic nor fully uniform in our case, the SoS method works well in practice in combining subprojections and restoring original complete projections.

II.E. Reconstruction

A multistage filtered backprojection (FBP) reconstruction technique was chosen to reconstruct all images, among other available reconstruction techniques. In the multistage FBP, the 3D image reconstruction is done in two two-dimensional (2D) inverse radon transform stages, which is faster than a single 3D backprojection.[25,26] A Ram–Lak filter cutoff of 0.5 was used to suppress the high frequency noise. The reconstruction field of view was chosen 3.0 cm. The reconstruction matrix size was 64 pixels along three dimensions for fast acquisition images (ESE-SB-I and MB-I protocols in Table I) and 128 pixels for the long acquisition (ESE-SB-II and MB-II).

II.F. Fitting T_2 decay

In order to determine T_2 value for each voxel, the intensity values in the five images from five different τ were selected and fitted to an exponential decay function. In order to avoid fitting empty voxels outside phantom, only voxels with first τ image intensity above 15% of maximum voxel intensity in the first τ image were chosen for fitting.

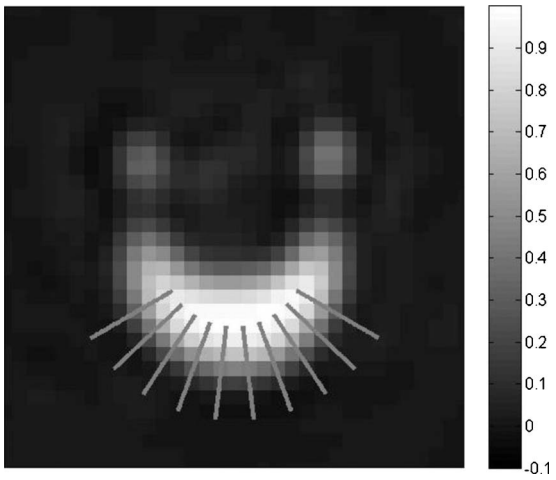

FIG. 4. Estimation of spatial resolution. The edge spread function width is estimated along the radial tracks shown in gray. The field of view here is 16 mm. The image shown taken by ESE-SB I scheme with 10 mT/m applied gradient.

II.G. Determining spatial resolution and T_2 uncertainty

The spatial resolution of the image is estimated by estimating the FWHM of the edge spread function, by fitting an error function to the intensity profile along the radial tracks around the cylindrical section of the bottle phantom. The technique is previously used for cw-EPR image resolution estimation.[27] Here we used the first τ ESE image, which has the best SNR, to fit the edge spread function. When the images are noisy the edge-fitting algorithm may fail and fit values may become too small or too large. To avoid fitting errors, any fit values below spatial-resolution lower bound (spin packet linewidth divided by the gradient magnitude) or twice higher than this value were discarded. Some of radial tracks used to determine spatial resolution are shown in Fig. 4.

The T_2 uncertainty is estimated by calculating the standard deviation of T_2 values in a uniform-intensity region of interest (ROI). The ROI was chosen in the following way: For each gradient, the fit masks from the three single-B and three multi-B images are chosen and have the two outer layers for 64^3 reconstruction, and four outer layers for the 128^3 reconstruction eroded to remove any edge effects in T_2 uncertainty determination. Next, any voxels corresponding to positions outside resonator cavity were discarded. Finally, the three single-B and three multi-B masks are overlapped, to choose only the voxels that have defined T_2 in all six images for every gradient.

Once the ROI is determined, the standard deviation of T_2 values in the ROI is calculated and reported as a measure of T_2 uncertainty or resolution. The T_2 resolution from the three images in each set is averaged, and the standard deviation of T_2 resolution values within each group is considered a measure of uncertainty in the T_2 resolution estimate.

II.H. One-dimensional experiments for noise power determination

1D projections along the axis of the resonator were acquired from the 200 μM Finland trityl phantom. A 50 mT/m gradient was applied along the major axis of the resonator. Together with the uniform profile of the phantom, the measurement provides us a uniform signal profile—up to $\pm 10\%$ due to B_1 nonuniformity—in the frequency range of importance (from -10 MHz to $+10$ MHz), where noise properties of the single- and multi-B projections can be investigated.

Besides constant gradient, acquisition conditions for single- and multi-B were as follows. For each method, 100 projections were acquired, with similar baseline acquisition for subtraction (once every four complete projections). The echo time and phase determination of the signal was done similarly in each case. AWF was measured and used to correct the frequency-domain single-B data and to combine and correct multi-B subprojections, as described earlier. For the purpose of comparison, single-B data with no AWF correction were also analyzed. All compared data were acquired at the same time. The projection noise $\sigma(f)_{\text{proj}}$ is determined as the standard deviation of the projection at each bin along the frequency axis from the 100 projections acquired using each method.

III. RESULTS

We compare the single-B and multi-B technique performance based on the following criteria: Image spatial resolution, T_2 resolution, and presence of image artifacts. The projection noise behavior obtained from 1D experiments is also compared. The imager AWF and a sample projection from single- and multi-B images are shown in Fig. 5.

III.A. Image spatial resolution

The results of spatial-resolution measurement for the two methods are given in Table II. As expected, larger gradients result in better spatial resolution. Furthermore, multi-B images have better estimated spatial resolution compared to single-B images. At larger gradients single-B images suffered from artifacts where the spatial resolution could not be determined reliably due to image distortions and artifacts. Sample images from each scheme are shown for 15 and 30 mT/m applied gradients in Figs. 6(a)–6(h).

III.B. T_2 resolution

For each image the estimated T_2 resolution is shown in Table II as well. As expected, at higher gradients T_2 standard deviations for both single-B and multi-B images increase, since SNR in each highly resolved voxel decreases and images become noisier. While 15 mT/m gradient T_2 uncertainty is smaller for the single-B image, at all higher gradients, multi-B images show clear improvement in T_2 resolution. It is also worth mentioning that when comparing single-B (ESE-SB) and multi-B (ESE-MB) images at similar acquisition times *and* similar spatial resolutions, the multi-B images have better T_2 resolutions. For instance, the ESE-MBII im-

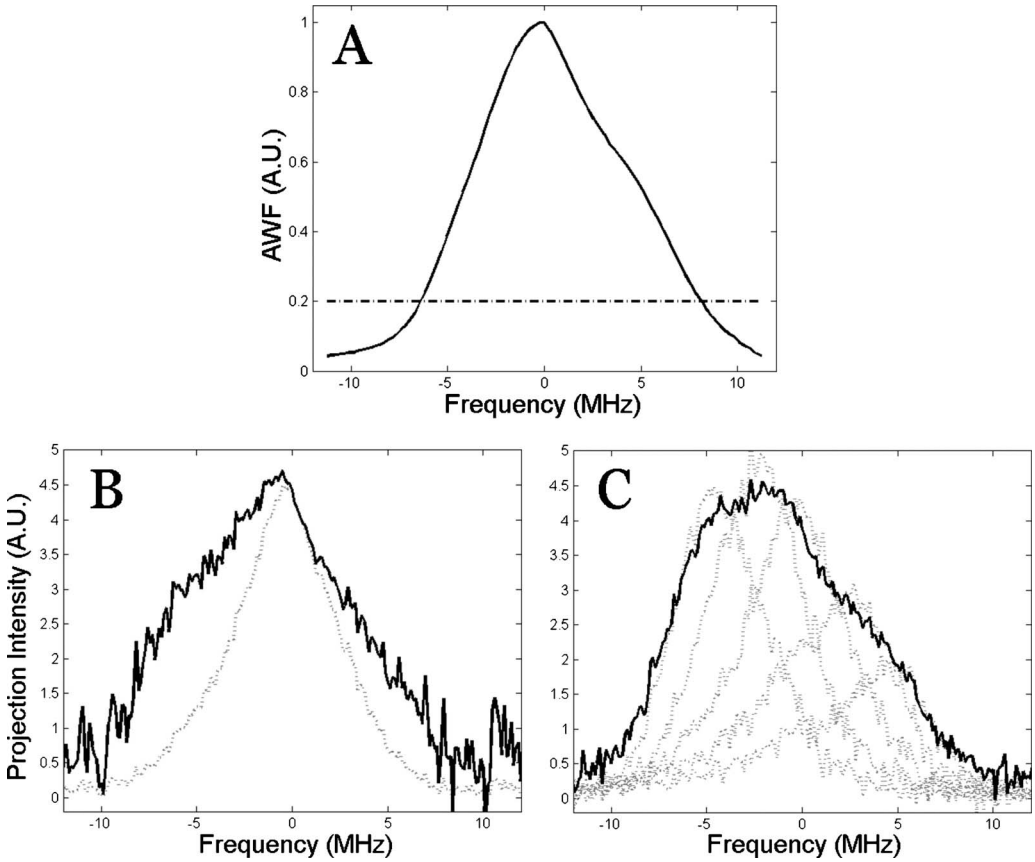

FIG. 5. (a) The ESE imager acquisition window function is shown in panel A (solid line). The dashed line indicates the 20% threshold used for AWF correction. For AWF values below the threshold value, a constant correction factor (5.0) is applied, to avoid noise amplification at peripheral frequencies. (b) A single-B projection from the ESE-SB-I 30 mT/m image is shown, both before applying the AWF correction (dotted line) and after AWF correction (solid line). (c) The same data acquired in the multi-B method, with the five subprojections (dotted) and the recovered complete projection (solid line). The inexact nature of the window function is seen in the comparison of (b) and (c), where a shoulder, seen in (b) is seen as a plateau in (c).

age at 15 mT/m has similar spatial resolution to the ESE-SB-II image at acquired with 20 mT/m gradient, i.e., about 1.02 mm, yet the T_2 uncertainty is clearly smaller for the multi-B image. Similar yet stronger argument can be made for the ESE-MB-I image at 15 mT/m gradient compared to the ESE-SB-I image acquired with 20 mT/m gradient, where the multi-B image is superior in terms of both spatial and T_2 resolutions.

III.C. Image artifacts

Multi-B images generally have diminished artifacts compared to corresponding single-B images. This is true especially at higher gradients where single-B images have nonuniform behavior around the periphery of the image, represented as concentric ring artifacts. Another artifact, related to the low frequency noise from system baseline which

TABLE II. Spatial and T_2 resolution for images taken using different ESE single- and multi-B protocols. The numbers inside parentheses indicate the standard error for each measurement.

	Spatial resolution, FWHM (mm)				T_2 resolution, standard deviation (μs)			
ESE Protocol	15 mT/m	20 mT/m	25 mT/m	30 mT/m	15 mT/m	20 mT/m	25 mT/m	30 mT/m
ESE-SB I	2.00	1.78	ND[a]	ND	0.24	0.49	0.64	0.76
	(0.09)	(0.07)			(0.05)	(0.04)	(0.09)	(0.13)
ESE-MB I	1.55	1.40	1.35	1.32	0.31	0.41	0.45	0.49
	(0.12)	(0.05)	(0.04)	(0.04)	(0.04)	(0.06)	(0.05)	(0.03)
ESE-SB II	1.37	1.01	ND	ND	0.35	0.54	0.81	0.96
	(0.08)	(0.10)			(0.05)	(0.04)	(0.04)	(0.15)
ESE-MB II	1.03	0.88	0.78	0.75	0.37	0.44	0.54	0.58
	(0.07)	(0.04)	(0.08)	(0.11)	(0.04)	(0.06)	(0.05)	(0.03)

[a]ND: Not determined, due to presence of image distortions and artifacts.

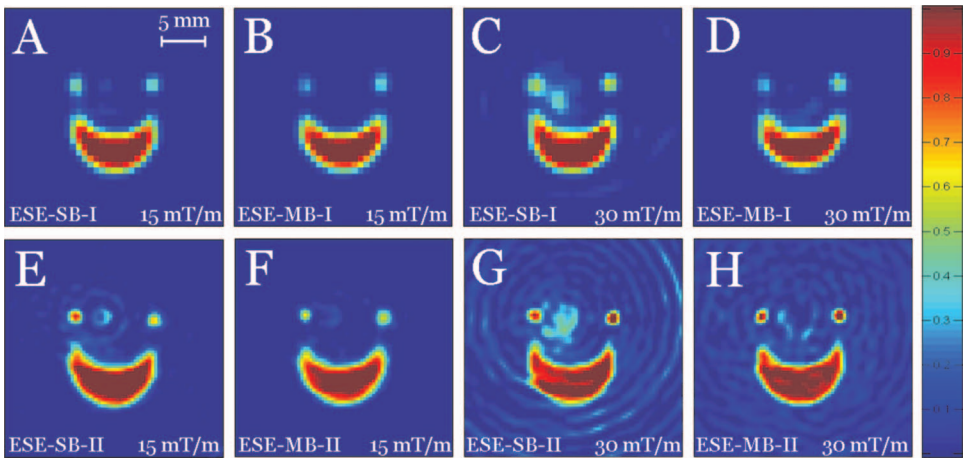

FIG. 6. Single-B versus multi-B. Spatial images acquired from the first τ image represented in color scale. The acquisition scheme and the applied gradient in indicated in the bottom left for each image. The field of view is 25 mm for all images shown. The center peak artifact is clearly visible in panels C, E, and G. The figures show only the region of the field of view containing the bottle and capillary tube cross sections. Since the phantom was not exactly centered at the gradient center, the location of the artifact is not at the center of the FOV. The artifacts seen in the figures are the a combination effect of nonstochastic noise and projection truncation, both of which are reduced in multi-B images.

appears as a hole or peak at the center of the field of view, is again less prominent in multi-B images. The center peak artifact is faintly present even in lower gradient single-B images [compare Figs. 6(e) and 6(f)]. Both center peak and concentric rings artifacts in the periphery get worse at higher gradients [compare Figs. 6(c), 6(d), 6(g), and 6(h)]. In all cases, the image artifact intensities are reduced when switching from single-B to the corresponding multi-B image acquisition.

III.D. Projection noise

In order to better understand the reason for the superiority of multi-B to single-B acquisition in the given gradient magnitude range, it is informative to compare the noise standard deviation at each frequency bin of the uniform projection from one dimensional experiments for the single- and multi-B methods, shown in Fig. 7. The raw single-B noise power is smooth except at ~0 and ~−15 MHz, where frequency is shown with respect to the central 250 MHz frequency. The zero-frequency noise peak can be attributed to ambient low frequency current and field fluctuations, and the −15 MHz noise is likely to be generated from components operating at approximately 235 MHz frequency such as computer CPUs. The profile is maximum at central frequency, which is expected since the imager is usually calibrated to transfer information (signal and noise) most effectively at the center frequency. The picture changes if the acquisition window function correction is applied to the data, as in Fig. 7(b). Note that for single-B projections, the correction is the inverse of AWF function up to a threshold, and uniform afterwards, as explained previously.[19] This correction results in strong enhancement of noise on the peripheral frequencies for the single-B, which does not occur as strongly for multi-B [Fig. 7(c)] as long as there are enough field steps covering the desired frequency range.

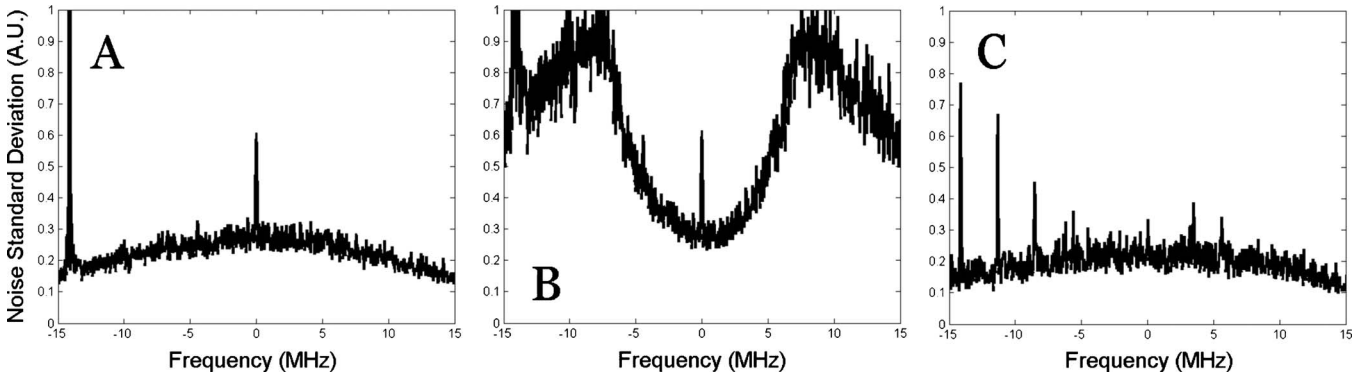

FIG. 7. Single-B versus multi-B projection noise. (a) Noise standard deviation at each frequency bin with 50 mT/m applied gradient for the uncorrected single-B projection. (b) The AWF-corrected single-B projection noise standard deviation. (c) The multi-B projection noise standard deviation. The peak at the center of the noise profile in (a) and (b) corresponds to small-frequency harmonic oscillations present in the echo signal. The large peak on left side of the spectrum in (a) is likely from the computer CPU operating at similar frequency to the acquisition frequency range. The same peak appears as several smaller peaks in the multi-B acquisition.

IV. DISCUSSION

A novel method for acquiring high resolution ESE images is demonstrated. Multi-B images can be acquired at higher gradients compared to standard ESE images, resulting in better spatial resolution with less susceptibility to image artifacts. It is important to note that no hardware or software changes are needed in the EPR image acquisition system in order to accommodate the multi-B imaging modality. The wisdom from MRI concerning multi-B acquisition is modest given the large MRI signal and the much larger signal bandwidth relative to the gradient bandwidth of the MRI system. Lee *et al.*[28] have described multiplex MRI acquisition using field stepped MRI. Idiyatullin *et al.*[29] also discussed a frequency swept tomographic acquisition.

It is worth mentioning that in our protocol for multi-B imaging, multi-B acquisition is faster than corresponding acquisition for single-B images (Table I). This is because the increased overhead from field shifting can be less than the time saved in acquiring baseline signals, since every baseline for multi-B is treated as a subprojection in terms of number of echo averages. Hence for the multi-B protocols used in this study (five subprojections per complete projection), multi-B images spend less time in baseline acquisition and are slightly shorter in experimental acquisition times than similar single-B images. The reason for treating baseline as a subprojection was that the baseline signal is not sensitive to the exact value of the field offset. Therefore, bandwidth extension was not needed for baseline acquisition in our multi-B schemes.

We also like to mention that ideally the spatial resolution of the single- and multi-B images acquired at the same gradients should be the similar. A major reason we observe degraded resolution for the single-B image at larger gradients is due to the projection truncation at peripheral frequencies. This results in image artifacts that affect the edge-fitting algorithm used for spatial-resolution determination.

The multi-B acquisition can be used when the bandwidth of the imager cannot be expanded otherwise. For example, by reducing the quality factor of the imaging resonator one could in principle expand the AWF width, yet this approach has certain limitations: The bandwidth is also determined by other components in the pulse generation and signal detection systems, such as the circulators and amplifiers. This problem aside, lowering the resonator Q would require larger rf power, which usually results in more data contamination due to the noise arising from power reflection due to any mismatch in the rf circuitry. If one is already operating at the maximum rf power, either the duration of excitation and refocusing pulses should increase—resulting in the loss of bandwidth—or one should operate at flip angles lower than 90° resulting in the loss of SNR.

It is important to mention drawbacks of the multi-B acquisition as well: One is the acquisition data size, which increases proportionally with the number of field steps, and can pose difficulty in storage and analysis of such data if enough storage or computational memory is not available. Another drawback is that the SNR per each subprojection is lower than the complete single-B projection SNR, which can be problematic for determining correct echo position and phase when the acquired data are very noisy, where more robust algorithms for echo position and phase determination should be used.

ACKNOWLEDGMENTS

We would like to acknowledge the work of our engineer, Mr. Subramanian Sundramoorthy in maintaining the EPR imaging acquisition system. This work is supported by NIH Grant Nos. P-41 EB002034 and R01-CA-98575.

[a]Author to whom correspondence should be addressed. Electronic mail: h-halpern@uchicago.edu

[1]L. J. Berliner and H. Fuji, "Magnetic resonance imaging of biological specimens by electron paramagnetic resonance of nitroxide spin-labels," Science **227**, 517–519 (1985).
[2]H. J. Halpern, D. P. Spencer, J. van Polen, M. K. Bowman, R. J. Massoth, A. C. Nelson, E. M. Dowey, and B. A. Teicher, "An imaging radiofrequency electron spin resonance spectrometer with high resolution and sensitivity for *in vivo* measurements," Rev. Sci. Instrum. **60**, 1040–1050 (1989).
[3]G. R. Eaton, S. S. Eaton, and K. Ohno, *EPR Imaging and in vivo EPR* (CRC, Boca Raton, FL, 1991).
[4]P. Kuppusamy, M. Chzhan, K. Vij, M. Shteynbuk, D. J. Lefer, E. Giannella, and J. L. Zweier, "Three-dimensional spectral-spatial EPR imaging of free radicals in the heart: A technique for imaging tissue metabolism and oxygenation," Proc. Natl. Acad. Sci. U.S.A. **91**, 3388–3392 (1994).
[5]M. Elas, B. B. Williams, A. Parasca, C. Mailer, C. A. Pelizzari, M. A. Lewis, J. N. River, G. S. Karczmar, E. D. Barth, and H. J. Halpern, "Quantitative tumor oxymetric images from 4D electron paramagnetic resonance imaging (EPRI): Methodology and comparison with blood oxygen level-dependent (BOLD) MRI," Magn. Reson. Med. **49**, 682–691 (2003).
[6]H. J. Halpern, C. Yu, M. Peric, E. Barth, D. J. Grdina, and B. A. Teicher, "Oxymetry deep in tissues with low-frequency electron paramagnetic resonance," Proc. Natl. Acad. Sci. U.S.A. **91**, 13047–13051 (1994).
[7]A. Bratasz, R. P. Pandian, Y. Deng, S. Petryakov, J. C. Grecula, N. Gupta, and P. Kuppusamy, "In vivo imaging of changes in tumor oxygenation during growth and after treatment," Magn. Reson. Med. **57**, 950–959 (2007).
[8]M. Elas, K. H. Ahn, A. Parasca, E. D. Barth, D. Lee, C. Haney, and H. J. Halpern, "Electron paramagnetic resonance oxygen images correlate spatially and quantitatively with oxylite oxygen measurements," Clin. Cancer Res. **12**, 4209–4217 (2006).
[9]M. Elas, R. Bell, D. Hleihel, E. D. Barth, C. McFaul, C. R. Haney, J. Bielanska, K. Pustelny, K.-H. Ahn, C. A. Pelizzari, M. Kocherginsky, and H. J. Halpern, "Electron paramagnetic resonance oxygen image hypoxic fraction plus radiation dose strongly correlates with tumor cure in fSa fibrosarcomas," Int. J. Radiat. Oncol., Biol., Phys. **71**, 542–549 (2008).
[10]Y. Deng, S. Petryakov, G. He, E. Kesselring, P. Kuppusamy, and J. L. Zweier, "Fast 3D spatial EPR imaging using spiral magnetic field gradient," J. Magn. Reson. **185**, 283–290 (2007).
[11]Y. Deng, G. He, S. Petryakov, P. Kuppusamy, and J. L. Zweier, "Fast EPR imaging at 300 MHz using spinning magnetic field gradients," J. Magn. Reson. **168**, 220–227 (2004).
[12]S. Subramanian, J. W. Koscielniak, N. Devasahayam, R. H. Pursley, T. J. Pohida, and M. C. Krishna, "A new strategy for fast radiofrequency CW EPR imaging: Direct detection with rapid scan and rotating gradients," J. Magn. Reson. **186**, 212–219 (2007).
[13]M. Tseitlin, A. Dhami, S. S. Eaton, and G. R. Eaton, "Comparison of maximum entropy and filtered back-projection methods to reconstruct rapid-scan EPR images," J. Magn. Reson. **184**, 157–168 (2007).
[14]J. W. Stoner, D. Szymanski, S. S. Eaton, R. W. Quine, G. A. Rinard, and G. R. Eaton, "Direct-detected rapid-scan EPR at 250 MHz," J. Magn. Reson. **170**, 127–135 (2004).
[15]J. P. Joshi, J. R. Ballard, G. A. Rinard, R. W. Quine, S. S. Eaton, and G. R. Eaton, "Rapid-scan EPR with triangular scans and Fourier deconvolution to recover the slow-scan spectrum," J. Magn. Reson. **175**, 44–51

(2005).
[16]C. Mailer, S. V. Sundramoorthy, C. A. Pelizzari, and H. J. Halpern, "Spin echo spectroscopic electron paramagnetic resonance imaging," Magn. Reson. Med. **55**, 904–912 (2006).
[17]S. Subramanian, N. Devasahayam, R. Murugesan, K. Yamada, J. Cook, A. Taube, J. B. Mitchell, J. A. Lohman, and M. C. Krishna, "Single-point (constant-time) imaging in radiofrequency Fourier transform electron paramagnetic resonance," Magn. Reson. Med. **48**, 370–379 (2002).
[18]M. M. Maltempo, "Differentiation of spectral and spatial components in EPR imaging using 2-D image reconstruction algorithms," J. Magn. Reson. **69**, 156–161 (1986).
[19]B. Epel, S. V. Sundramoorthy, C. Mailer, and H. J. Halpern, "A versatile high speed 250-MHz pulse imager for biomedical applications," Concept Magn. Reson., Part B **33B**, 163–176 (2008).
[20]J. H. Ardenkjaer-Larsen, I. Laursen, I. Leunbach, G. Ehnholm, L. G. Wistrand, J. S. Petersson, and K. Golman, "EPR and DNP properties of certain novel single electron contrast agents intended for oximetric imaging," J. Magn. Reson. **133**, 1–12 (1998).
[21]T. J. Reddy, T. Iwama, H. J. Halpern, and V. H. Rawal, "General synthesis of persistent trityl radicals for EPR imaging of biological systems," J. Org. Chem. **67**, 4635–4639 (2002).
[22]V. S. Subramanian, E. Boris, M. Colin, and J. H. Howard, ""A passive dual-circulator based transmit/receive switch for use with reflection resonators in pulse electron paramagnetic resonance," Concept Magn. Reson., Part B **35B**, 133–138 (2009).
[23]K. H. Ahn and H. J. Halpern, "Spatially uniform sampling in 4-D EPR spectral-spatial imaging," J. Magn. Reson. **185**, 152–158 (2007).
[24]E. G. Larsson, D. Erdogmus, R. Yan, J. C. Principe, and J. R. Fitzsimmons, "SNR-optimality of sum-of-squares reconstruction for phased-array magnetic resonance imaging," J. Magn. Reson. **163**, 121–123 (2003).
[25]R. K. Woods, W. B. Hyslop, R. B. Marr, and P. C. Lauterbur, in *EPR Imaging and In Vivo EPR*, edited by G. R. Eaton, S. S. Eaton, and K. Ohno (CRC, Boca Raton, FL, 1991), pp. 91–117.
[26]B. B. Williams, X. Pan, and H. J. Halpern, "EPR imaging: The relationship between CW spectra acquired from an extended sample subjected to fixed stepped gradients and the radon transform of the resonance density," J. Magn. Reson. **174**, 88–96 (2005).
[27]K. H. Ahn and H. J. Halpern, "Simulation of 4D spectral-spatial EPR images," J. Magn. Reson. **187**, 1–9 (2007).
[28]K. J. Lee, M. N. Paley, I. D. Wilkinson, and P. D. Griffiths, "Magnetic resonance imaging with stepped B0 fields," Magn. Reson. Imaging **21**, 625–629 (2003).
[29]D. Idiyatullin, C. Corum, J.-Y. Park, and M. Garwood, "Fast and quiet MRI using a swept radiofrequency," J. Magn. Reson. **181**, 342–349 (2006).